Intercalation of Ca into a Highly Defective Manganese Oxide at Room Temperature

Bob Jin Kwon[1,2]*, Liang Yin[2,3], Christopher J. Bartel[2,4,5], Khagesh Kumar[6], Prakash Parajuli[2,7], Jihyeon Gim[1], Sanghyeon Kim[1,2], Yimin A. Wu[2,7], Robert F. Klie[2,7], Saul H. Lapidus[2,3], Baris Key[1,2], Gerbrand Ceder[2,4,5], and Jordi Cabana[2,6]*

[1]Chemical Sciences and Engineering Division Argonne National Laboratory, Lemont, IL 60439, United States

[2]Joint Center for Energy Storage Research, Argonne National Laboratory, Lemont, IL 60439, United States

[3]X-ray Science Division, Advanced Photon Source, Argonne National Laboratory, Lemont, IL, 60439, United States

[4]Department of Materials Science and Engineering, UC Berkeley, Berkeley, CA, 94720, United States

[5]Materials Science Division, Lawrence Berkeley National Laboratory, Berkeley, CA, 94720, United States

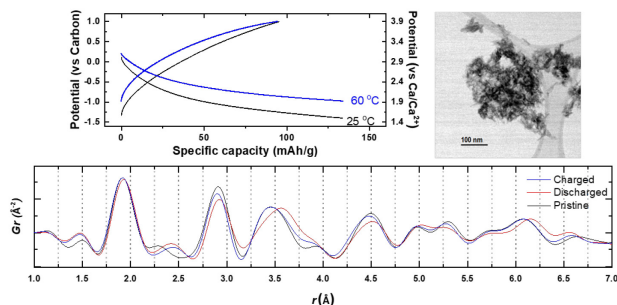[6]Department of Chemistry, University of Illinois at Chicago, Chicago, IL 60607, United States

[7]Department of Physics, University of Illinois at Chicago, Chicago, IL 60607, United States

Corresponding Author

*E-mail: bkwon@anl.gov, jcabana@uic.edu

1

ABSTRACT

The utilization of oxide frameworks as intercalation cathodes for non-aqueous Ca-ion batteries potentially unlocks a new energy storage system that delivers high energy density. However, the slow kinetics of Ca^{2+} in oxide electrodes strongly handicaps their activity and reversibility at room temperature. Herein, nanocrystals of layered MnO_x containing a high concentration of atomic defects and lattice water are shown to have remarkable electrochemical activity towards Ca^{2+}, amounting to a capacity of ~130 mAh/g at room temperature. Multimodal characterization revealed the notable degree of intercalation by probing the structural, compositional and redox changes undertaken by the defective MnO_x nanocrystals. The results suggest that the existence of atomic defects and lattice water played a role in improving Ca^{2+} diffusivity in the oxide. These outcomes reaffirm the prospects for functional Ca-ion batteries using oxide cathodes under moderate conditions.

INTRODUCTION

Advances in rechargeable batteries operated by a path of intercalation of multivalent ions open new prospects for high-energy storage systems as an alternative to the current Li-ion batteries.[1-3] Multivalent batteries potentially deliver higher volumetric energy density at a lower cost with improved safety compared to Li-ion batteries.[1,3] Among the possible choices of multivalent metal, Ca has the closest reduction potential (-2.87 V *vs.* standard hydrogen electrode, SHE) to that of Li (-3.04 V *vs.* SHE), providing a higher output potential than other multivalent options.[4] Moreover, the larger ionic radius of Ca^{2+} shows a relatively smaller charge density, which decreases the strength of polarization in solid lattices compared to other divalent ions Mg^{2+} and Zn^{2+}, potentially manifesting in better kinetics.[5] These favorable aspects, along with high elemental abundance and low environmental concern, are propelling interest toward exploring chemistries for Ca-ion batteries.

The most critical issue hampering a practical device based on shuttling of Ca^{2+} is the poor kinetics of the electrochemical reaction in the cathode at moderate temperatures. The leading explanation for this obstacle is that, even with a relatively smaller charge density than Mg^{2+}, there is still unacceptably strong electrostatic cation-cation repulsion and cation-anion attraction limiting Ca^{2+} diffusion through the solid framework.[6,7] Thus, it is essential to design and discover intercalation cathodes with sufficient cation mobility to approach the theoretical limits of the concept.[3,7] Reversible intercalation of Ca^{2+} has been attempted in a variety of hosts, such as metal chalcogenides, polyanionic and organic compounds.[8-10] Among these candidates, reversible reactions have been observed in a few frameworks composed of soft anions (e.g., S^{2-} and Se^{2-}).[11-13] The identity of the anions in the host framework is critical to tuning the reaction potentials.[3,7,14] In general, oxides exhibit higher redox potentials than compounds with softer anions,

emphasizing the necessity of exploring them as hosts.[3, 7] So far, a few oxides have been proposed from theoretical calculations, but limited evidence of Ca^{2+} intercalation particularly in dry non-aqueous electrolytes has been observed experimentally.[6, 15] Consequently, a primary question becomes whether intercalation of Ca^{2+} into an oxide is fundamentally reachable at high potentials and moderate temperatures in a dry non-aqueous electrolyte that also enables pairing with Ca metal anodes ultimately. Unfortunately, few electrolytes can operate with Ca metal anodes, severely limiting the choices to build an electrochemical cell with analytical power.[16]

The polymorphism of MnO_2 provides a potentially attractive playground for exploration of structures that are favorable for intercalation because their geometries can be tuned, offering a diversity of sites where they could accommodate multivalent cations.[17, 18] The packing of MnO_6 octahedral units can enable a spectrum of layered to tunnel structures with a sublattice of equivalent interstitial sites that not only host intercalating cations but also but also H_2O molecules in the MnO_2 frameworks.[18, 19] Such H_2O is proposed to play a positive role in shielding the effective charges of intercalant cations, and thereby enhance reaction kinetics and modify potentials.[20, 21] The capability of MnO_2 polymorph containing lattice H_2O as an intercalation host for Mg^{2+} and Zn^{2+} was proved in dehydrated non-aqueous electrolytes[22, 23], but there still scarce details of the possible mechanism in electrochemical Ca activity in a MnO_2 polymorph.[24]

Another common approach to enhance kinetics involves reducing particle size, which shortens the length of bulk diffusion and maximizes the reactive surface area.[22, 25, 26] It has been reported that nanoscale oxides can enhance the kinetics of Mg^{2+} transport, suggesting the feasibility of the strategy for divalent cations.[22, 25] Methods to reduce particle size can also introduce atomic defects,[27, 28] which are predicted to significantly affect the kinetics of Ca^{2+} intercalation in oxides by altering the topology of the diffusion path.[3, 29] Encouragingly, in previous reports, defects were

found to enhance the electrochemical (de)intercalation of Mg^{2+} in $MgCr_2O_4$ and $FePO_4$.[26, 30] However, the specific outcome of inducing defects will depend on the relationship between the defects and the diffusion pathway, a rule of design that has not yet been fully explored experimentally.[3]

Here, we probe the ability of nanocrystals of MnO_x containing mixed-valent Mn, lattice water and crystallographic defects to undergo electrochemical reactions in a dry non-aqueous electrolyte involving Ca^{2+} cations. Pair distribution function (PDF), microscopic and spectroscopic analyses, provided insight into the intricate local ordering and chemistry in the complex nanocrystals. Multimodal characterization of key states cycled in a non-aqueous electrolyte at room temperature reveal structural, compositional, and electronic changes in the bulk that are consistent with reversible intercalation of Ca^{2+}. Calculated barriers for Ca migration estimated with no atomic defects or crystal waters suggest that their existence enables the observed electrochemical properties. These observations build a fundamental step forward in the capability of oxide lattices to reversibly intercalate Ca^{2+} in a dry non-aqueous electrolyte at moderate temperatures. They enrich our understanding of intercalation chemistry and attain a milestone toward a high-energy Ca battery by demonstrating electrochemical activity in oxides at room temperature.

EXPERIMENTAL SECTION

Synthesis of MnO$_x$

Pristine MnO_x nanoparticles were synthesized by a redox sol-gel reaction in distilled water. Sodium permanganate ($NaMnO_4$, product no. 225851 in Sigma-Aldrich) was used as a precursor, and disodium salt of Fumaric acid ($C_2H_2O_4Na_2$, product no. F1506 in Sigma-Aldrich) was

introduced as a reducing agent. A 200 mL of 0.25 M $NaMnO_4 \cdot H_2O$ solution was mixed with 50 mL of 0.333 M $C_2H_2O_4Na_2$ and stirred vigorously for 1 hour. The mixture was then sonicated for 5 hours. A disproportionation reaction was subsequently induced by the addition of 10 mL of 2.5 M sulfuric acid. The colloidal solution was further stirred vigorously at room temperature overnight. After washing unreacted species multiple (>5) times by centrifugation, the resultant powders were dried in a vacuum oven at 80 °C overnight.

Density functional theory calculations

DFT calculations were performed using the Vienna Ab Initio Simulation Package.[31] The generalized gradient approximation as formulated by Perdew, Burke, and Ernzerhof and the projector augmented-wave method were used with an energy cut-off of 520 eV and at least 1000 k-points per reciprocal atom. Mn $3d^64s^1$, O $2s^22p^4$, and Ca $3p^64s^2$ were treated explicitly with the remainder of electrons treated with pseudopotentials. Geometry optimizations were converged to 10^{-6} eV for electronic relaxations and 0.01 eV/Å for ionic relaxations. Structures were calculated in ferromagnetic and antiferromagnetic configurations, with the latter being the lowest energy for all three structures (birnessite, hollandite, and todorokite), in agreement with previously reported results.[32] Nudged elastic band (NEB) calculations were performed using the climbing image approach, with each image converged to 10^{-4} eV for electronic relaxations and 0.05 eV/Å for ionic relaxations.

Characterization

Room temperature synchrotron X-ray total scattering data were collected on beamline 11-ID-B at the Advanced Photo Source (APS), ANL. The rapid-acquisition PDF method[33] was used with an X-ray energy of 58.6 k eV (λ = 0.2115 Å). A PerkinElmer amorphous Si two-dimensional image-plate detector (2048 × 2048 pixels and 200 × 200 μm pixel size) was used at a distance of ~180 mm. The two-dimensional data were converted to one-dimensional XRD data using the GSAS-II software. PDF data were obtained from Fourier transformation of the background and Compton scattering corrected data *S(Q)* in *xPDFsuite* software over a *Q* range of 1-19 Å^{-1}. Local structure refinements using X-ray and neutron PDFs were carried out in *TOPAS* Academic, version 6. Partial PDF patterns were calculated using *PDFgui* software.

Ca K-edge and Mn K-edge X-ray absorption spectroscopy (XAS) was collected at beamline 20-BM and 9-BM-C respectively at the Advanced Photon Source at Argonne National Laboratory. The incident beam energy was selected by using a Si (111) monochromator. The measurements were done in fluorescence mode using a multi-element, energy dispersive germanium and a four-element vortex detector, for the Ca K- and Mn K-edge, respectively. The spectrum of CaO was used for alignment. The energy calibration at the Mn K-edge was done using a Mn foil scan collected simultaneously with the samples. Data reduction and analysis were performed using the Athena from the DEMETER package. The integration method was used to determine edge position, as described in the literature.[34] A value of μ_1 = 0.18 was used to minimize contributions from the pre-edge features and μ_2 = 1.00 was used to reduce effect from strong white line.

Scanning transmission electron microscopy (STEM), as well as electron energy loss spectroscopy (EELS) and energy dispersive X-ray spectroscopy (EDX) were performed on an aberration-corrected JEOL JEM-ARM200CF operated at 200 kV which can achieve a spatial resolution of ~73 pm. The ARM200CF is equipped with a cold-field emission gun, providing an

energy resolution of 350 meV. EDX spectra were collected by an Oxford X-Max 100TLE windowless silicon drift EDX detector, and EELS were collected using the Gatan Quantum imaging filter with a convergence angle of 30 mrad and a collection angle of 35 mrad.

Electrochemical measurement

The electrochemical performance was evaluated on a composite containing the MnO_x as a working electrode. Electrode slurries were prepared by mixing the active material, Timcal C45 carbon, and 6 wt% of a binder solution consisting of polyvinylidene difluoride (PVDF, Solvay) in N-methylpyrrolidone (NMP, Sigma-Aldrich) with a ratio of 6:2:2. Then, the slurries were cast on a stainless steel foil (Alfa Aesar, Type 304, 0.002 inch thickness), which has shown less reactivity with corrosive electrolytes than other foils such as Al and Cu.[35] Then, it was dried under vacuum at 80 °C overnight to evaporate NMP. The loading level of active oxide in the dry electrodes was set to around 2~3 mg/cm^2. Circular pieces of electrodes with a diameter of 3/8 inch were punched and assembled in two-electrode coin cells in a glovebox filled with inert Ar gas. The levels of water and oxygen were ≤ 1.0 ppm. Electrochemical measurements were conducted in 0.5 M calcium Bis(trifluoromethane sulfonyl)imide) (Ca(TFSI)$_2$, 99.5 %, Solvionic) dissolved in diglyme (99.5 %, Sigma Aldrich). The Ca(TFSI)$_2$ salt was dried at 120 °C under vacuum overnight before being dissolved in diglyme. The water content of the solvent was confirmed to be less than 15 ppm via Karl Fischer titration (Mettler Toledo DL39 Karl Fischer coulometer). The counter electrode was activated carbon, which was prepared by mixing activated carbon, Timcal C45 carbon and PVDF with a ratio of 8:1:1 in weight percent. The high specific surface area of the activated carbon gives rise to sufficient double-layer charging to match the charge needed to cycle

the cathode. Glass microfiber filters (VWR 28297-289) were used as a separator in the coin cell experiment. Electrochemical measurements were performed on a Biologic VMP3 at 25 and 60 °C. The potentials in this report are referenced to the activated carbon. The rate, C/n, was defined as the current density required to achieve a theoretical capacity of MnO_2, C = 280 mAh/g, in n hours, assuming the reaction of $0.5Ca^{2+} + MnO_2 \leftrightarrow Ca_{0.5}MnO_2$. Electrodes harvested for further characterization were washed multiple times with acetonitrile to remove electrolyte residues.
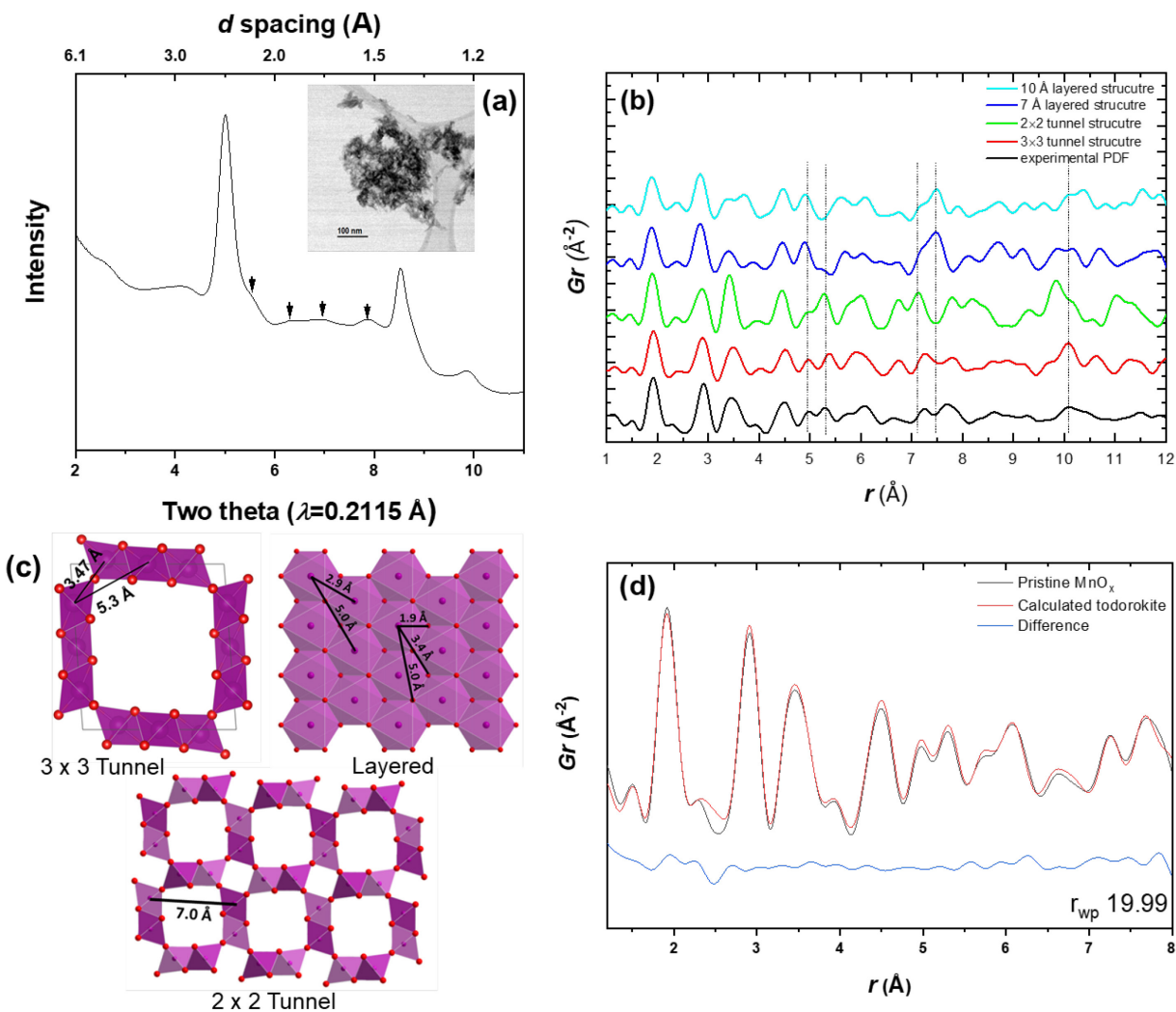
RESULTS AND DISCUSSION

Figure 1. (a) Synchrotron powder XRD pattern; (b) experimental and theoretical PDF patterns of pristine and model polymorphs for comparison; (c) model polymorph structures of MnO_2; (d) a representative fit of the pair distribution function data for MnO_x using a todorokite model. The inset in Figure 1a is a representative image of MnO_x nanocrystals.

Structural characterization of defective MnO_x nanocrystals. Nanoparticles of MnO_x were synthesized *via* an aqueous sol-gel reaction involving reduction of sodium permanganate, followed by treatment in an acidic solution to induce atomic and electronic defects.[22, 36] The amount of water in the lattice and/or on the surface of MnO_x was estimated by thermal analysis, which amounted to $n \approx 0.6$ when assuming the formula $MnO_2 \cdot nH_2O$.[22] It is also possible that the value included a contribution from lattice protons, forming -OH groups within the framework, which could not be evaluated directly. The synchrotron diffraction pattern of pristine MnO_x (**Figure 1a**) indicated an extremely low crystallinity with broad reflections at *d*-spacing of ~2.4 Å, with a tail at a higher angle (~1.4 Å). These reflections could be indexed as corresponding to the (*11, 20*) and (*31, 02*) families of planes of a typical layered phyllomanganate. The ratio of *d*-spacing between the two main peaks was ~1.7, close to $\sqrt{3}$, possibly indicating hexagonal-like in-plane symmetry of the oxide.[37, 38] A small bump at ~2.5° (~4.8 Å) corresponds to (*00l*) reflections, indicating the limited coherence along the stacking direction. The MnO_x nanoparticles were only a few nanometers along the c-axis, according to transmission electron microscopy (**Figure 1a**), leading to the limited coherent scattering along this dimension, consistent with the XRD patterns. In addition, there were broad and weak humps reminiscent of the 3×3 tunnel structure of todorokite (JCPDS 38-475), at *d*-spacings of ~2.2 Å (*2, 1, -2*), ~1.9 Å (*2, 1, -3*), ~1.7 Å (*3, 1, 3*) and 1.5 Å (*2, 1, -5*) (see arrows in **Figures 1** and **S1**).[28] It is typically difficult to distinguish layered phyllomanganate from tunnel

todorokite because of their topotactic relationships and the existence of intermediates; transformations between them are commonly observed in the literature.[39]

Overall, the XRD pattern highlights the complex local structure of the nanocrystalline oxide. Further insight was gained by analyzing its pair distribution function (PDF) (**Figure 1b~d**). Fast damping of the PDF peaks again reflects the small particle sizes of MnO_x, with structural coherence only over a few nanometers (**Figure S2**). A comparison of the experimental X-ray PDF with calculated PDF patterns of reported polymorphs of MnO_2 is shown in **Figure 1b**. The first peak at 1.92 Å corresponds to Mn-O correlations in MnO_6 octahedra, while the second peak at 2.90 Å refers to Mn-Mn and O-O correlations induced by their sharing of edges (**Figure 1b**). The position of Mn-O and nearest neighbor Mn-Mn pairs in edge-sharing octahedra is mostly indistinguishable in the different polymorphs of MnO_2 that could conceivably form.[37] In contrast, their ratio of intensities (I_{Mn-O}/I_{Mn-Mn}) is generally higher for tunnel than layered structures (**Figure 1b**). An increase in the intensity ratio compared to the layered polymorphs was found in the experimental PDF, implying that the local structure of MnO_x has a substantial concentration of intralayer vacancies, leading to a decrease in short Mn-Mn contacts.

The experimental PDF of MnO_x displays prominent peaks at ~3.5 and ~5.3 Å, which are generally regarded as a distinguishing feature of tunnel frameworks compared to layered structures (**Figure 1c**).[38] These peaks arise through the contact between a corner Mn in one of the tunnel walls and the first and second Mn, respectively, in the perpendicular wall (**Figure 1b** and **c**). In a layered structure, such perpendicular arrangements can be introduced when an intralayer Mn migrates between the layers, leaving a vacancy behind.[27, 38] Accordingly, this feature is seen to gradually intensify with the concentration of such interlayer defects during the transformation to a crystallized tunnel structure.[39] Overall, compared with modeled patterns of different possible

MnO$_2$ polymorphs, the local structure shown by the PDF data of the synthesized MnO$_x$ sample (1-8 Å) is a reminiscent of todorokite with 3×3 tunnels. Fits of the PDF data were attempted using either a single todorokite phase or a todorokite/layered mixture (**Figure 1d** and **Figure S3**). A good fit of the experimental PDF data (1-8 Å) with the local features of the 3×3 tunnel structure was achieved after refinement, converging with the final R_{wp} 19.99% (**Figure 1d**). Introducing the layered framework into the fitting improved the R_{wp} to 19.08% (**Figure S3**). The small improvement could be ascribed to the deviations from a regular tunnel structure, for instance, forming chains longer than 3 Mn between walls, before an intralayer vacancy associated with the wall is present.

Indeed, important characteristic features of periodic (ordered) 2×2 and 3×3 motifs are either missing or very weak. These include largely missing peaks at ~7.0 and ~8.4 Å, corresponding to the tunnel width and diagonal in a 2×2 structure, and a weaker than predicted intensity at ~10 Å, associated to the tunnel width in a 3×3 arrangement. Furthermore, the intensities of PDF peaks above 9.5 Å damped fast, which indicates the weak correlation between interlayer linkage at length scales beyond one unit cell, in agreement with the absence of (*001*) reflections in the XRD pattern. Therefore, the synthesized MnO$_x$ could be described as a defective layered polymorph containing abundant tunnel walls, but which are unevenly distributed between the MnO$_2$ layers,[27] rather than forming the regular 3×3 arrays characteristic of crystalline todorokite. The weak intensity at ~7 Å specifically implies that the distance between interlayer Mn is longer than across the 2×2 tunnel walls of hollandite (α-MnO$_2$). Irregular distributions of chain lengths are also common in fully crystallized todorokite,[40, 41] so the lack of coherence observed here indicates even greater deviations from a tunnel structure, towards an irregular layered framework.
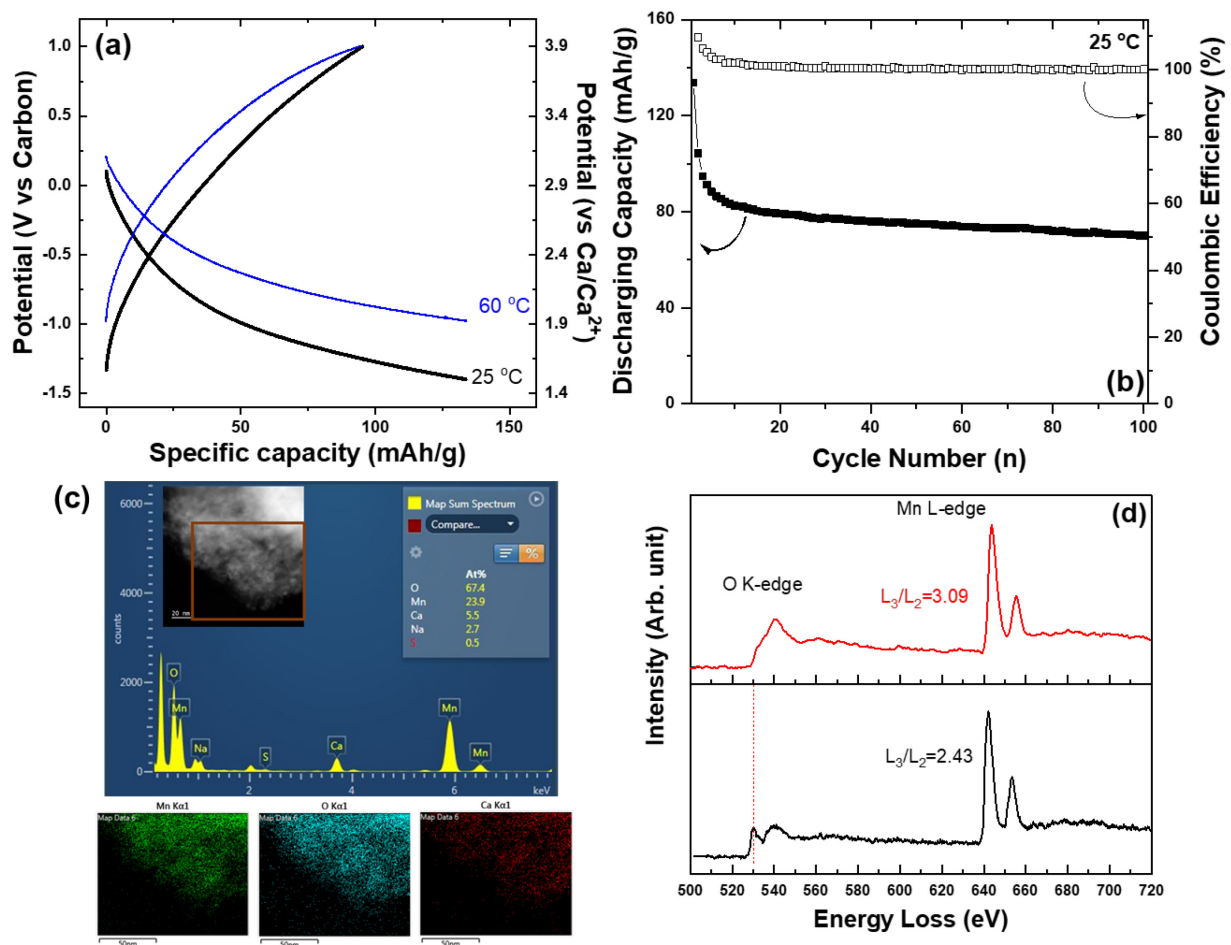
Figure 2. (a) Potential versus capacity profiles of MnO_x cycled in 0.5 M $Ca(TFSI)_2$ dissolved in

diglyme at 25 °C (black) and 60 °C (blue), and (b) cycling performance of the cathode at a rate of

C/25 at 25 °C. (c) EDX mapping of calciated MnO_x and (d) EELS of the pristine and calciated

MnO_x nanoparticles. (Black: pristine and red: discharged)

Evaluation of electrochemical Ca^{2+} activity at moderate temperatures. The electrochemical properties were measured at both 25 °C and 60 °C in a half-cell consisting of quasi carbon reference[42, 43] and MnO$_x$ working electrode with a dry non-aqueous Ca electrolyte, 0.5 M Ca(TFSI)$_2$ dissolved in diglyme (**Figure 2a**). The cut-off potentials were selected by considering the electrochemical stability of the electrolyte. The cathodic reaction at 25 °C proceeded from around -0.25 V (*vs.* carbon), and a discharge capacity of ~133 mAh/g was achieved at -1.4 V (*vs.* carbon), which could be converted to a potential of ~1.5 V *vs.* Ca/Ca^{2+} following calibration methods in the literature.[44] The profile of the cathodic reaction was overall sloping, centered at around -1.0 V *vs.* carbon (~1.9 V *vs.* Ca/Ca^{2+}). The discharge capacity corresponds to roughly 0.25 moles of Ca^{2+} per mole of host, assuming a theoretical formula of MnO$_2$. Nonetheless, it is worth noting that structural results indicate that the actual x in MnO$_x$ is below 2 due to the presence of numerous defects and vacancies, presenting large uncertainty in the calculation of the actual theoretical capacity. Upon subsequent charging, a specific capacity of ~95 mAh/g was achieved up to 1.0 V (*vs.* carbon), which was ~3.9 V (*vs.* Ca/Ca^{2+}). The profile was again sloping, with a midpoint at around 0 V *vs.* carbon (~2.9 V *vs.* Ca/Ca^{2+}).

The cells were tested at a raised temperature (60 °C) to probe reaction kinetics (**Figure 2a**). A similar capacity was reached at -1.0 V upon the cathodic reaction, ~0.4 V higher than the 25 °C experiment, implying enhanced kinetics. On the other hand, a similar charge capacity was achieved at the same cut-off potential up to 1.0 V. Overall, the average potential of the process was ~0.25 V higher than that cycled at room temperature. The cycling curve of MnO$_x$ at 25 °C showed a gradual decrease in the discharge capacity (**Figure S4**), to ~70 mAh/g after 100 cycles (**Figure 2b**). Despite the drop of capacity, the result is encouraging in that it demonstrates that Ca^{2+} intercalation in oxides is possible at moderate temperatures. The electrode after 100 cycles was

analyzed by X-ray diffraction to track any formation of secondary phases possibly produced by undesired reaction pathways, such as conversion (**Figure S5**). No visible secondary phases were detected in the diffraction, implying a consistent intercalation reaction.

Elemental mapping and valence state scanning at spatial resolution. The content and elemental distribution in the pristine and discharged MnO_x electrodes were estimated by EDX mapping through the nanocrystalline particles (**Figure 2c** and **S6**). Pristine MnO_x showed evidence of Na at a ~0.2 of Na/Mn ratio generated during the synthesis (**Figure S6**), which was maintained after discharge (**Figure S7**). In the discharged electrode, the Ca/Mn ratio was ~0.23, compared to ~0.25 estimated from the corresponding discharge capacity (**Figure 2c**). The minor signal of sulfur (S^{2-}), an element in the anion group of $Ca(TFSI)_2$, indicated most of the residual electrolyte was removed by washing the electrode, implying that the captured Ca signal was mostly generated by Ca^{2+} species bearing with MnO_x (**Figure 2c**). Moreover, the amount of Ca on multiple large areas throughout the electrode was estimated by SEM-EDX (**Figure S7**), amounting to a Ca/Mn ratio of ~0.3. A significant decrease of Ca signal upon the anodic reaction was detected on the electrode while the residual Na^+ existing in the pristine was also removed (**Figure S7**).

Electron energy loss spectra (EELS) at the Mn L- and O K-edges were collected across both pristine and calciated MnO_x (**Figure 2d** and **S8**). The most prominent observation at the O K-edge was that the threshold of absorption was lowered due to filling of the hybridized O_{2p}-Mn_{3d} orbital, suggesting a reduction of Mn.[45] The lowered signal in the pre-edge could be explained by the spin-down exchange split bands being almost occupied in the electronic configuration of reduced Mn.[45] Moreover, variations in the valence states of Mn were estimated by examining a relative peak ratio of Mn L_3 to L_2 edge which is indicative of the electronic environment of Mn ions. These edges correspond to dipole-allowed transitions from Mn 2p to unoccupied 3d orbitals, separated by the

spin-orbital interaction of the Mn 2p core hole.[46] A bigger branching ratio (L_3/L_2) indicates the electronic environment evolved toward a reduced state of Mn. The ratios for pristine and calciated MnO_x were 2.43 and 3.09, respectively. It implies a relatively reduced state of Mn upon Ca^{2+} intercalation.[47]
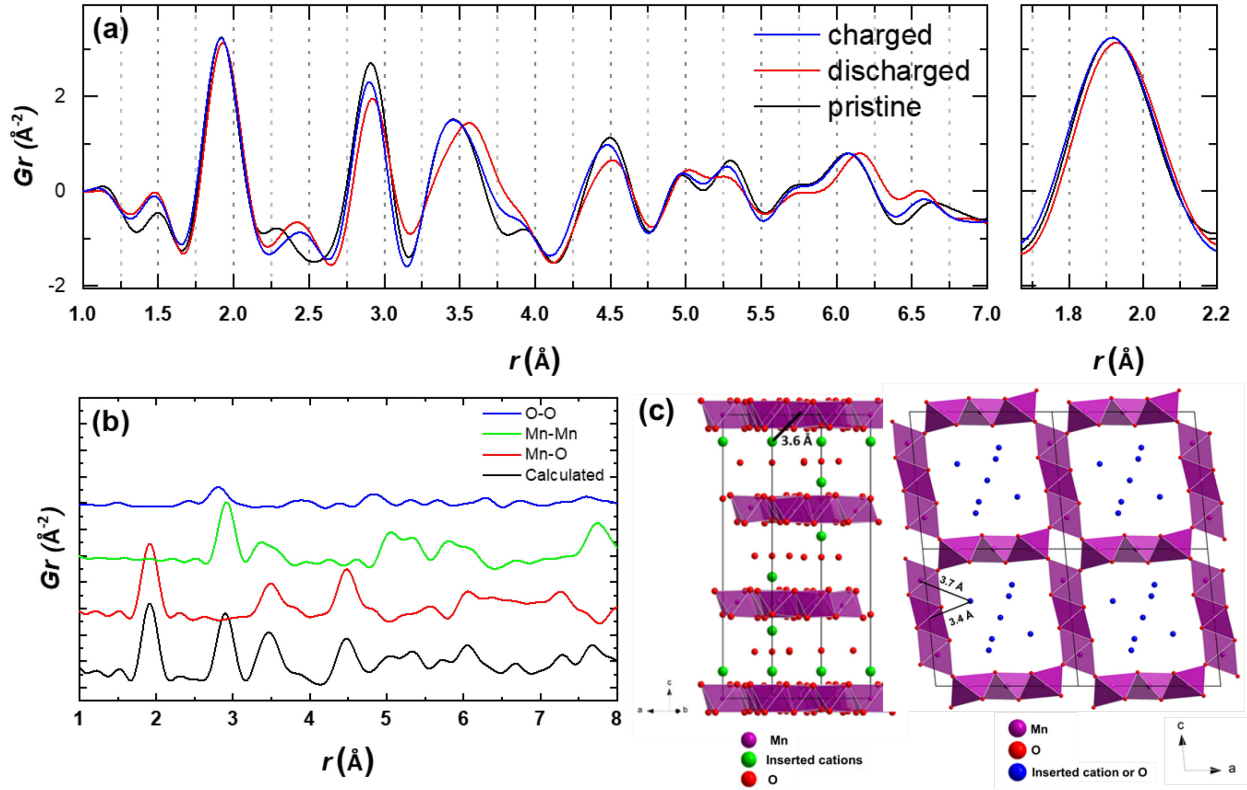

Figure 3. (a) PDF analyses for MnO_x at various states of charge prepared at 25 °C. (Black: pristine, red: discharged, and blue: charged MnO_x electrodes) (b) Calculated PDF patterns of todorokite MnO_2 and partial PDF patterns of selected atomic pairs. (c) Structure models of layered MnO_2 (left) and 3 × 3 tunnel MnO_2 (right) with inserted cations.

X-ray pair distribution function (PDF) analysis. X-ray PDF analyses were performed on the electrodes recovered from different states of charge (**Figure 3a**), after subtracting the background of electrode components such as carbon and binder. All the peaks with contributions from Mn-O pairs within and between MnO_6 octahedra i.e., at ~1.9, 3.6 and 4.5 Å (**Figure 3a and b**), underwent a reversible shift to higher values upon reduction. The second peak (~2.87 Å) was also affected by the electrochemical reaction, implying elongation and contraction of the Mn-Mn pairs in neighboring face-sharing octahedra. The pair at ~3.6 Å was could also reflect either the inserted Ca^{2+} into the interlayer of layered MnO_2 or the corner position in 3×3 tunnel MnO_2 structure as indicated in the proposed models (**Figure 3c**).[48] Furthermore, it was also detected that the intensity of the Mn-Mn pair at ~5.3 Å, the signature peak of Mn-Mn contacts across the corner formed by the walls of tunnel structures, was weakened while the peak at ~5.0 Å was intensified. Considering that these peaks are sensitive to the concentration of interlayer Mn/intralayer vacancies in a phyllomanganate model, it is possible partial relocation of Mn in the lattice may occur simultaneously together with intercalation of Ca^{2+}.[49] The mobility of reduced Mn species in oxide lattices has been well justified on theoretical grounds.[50]
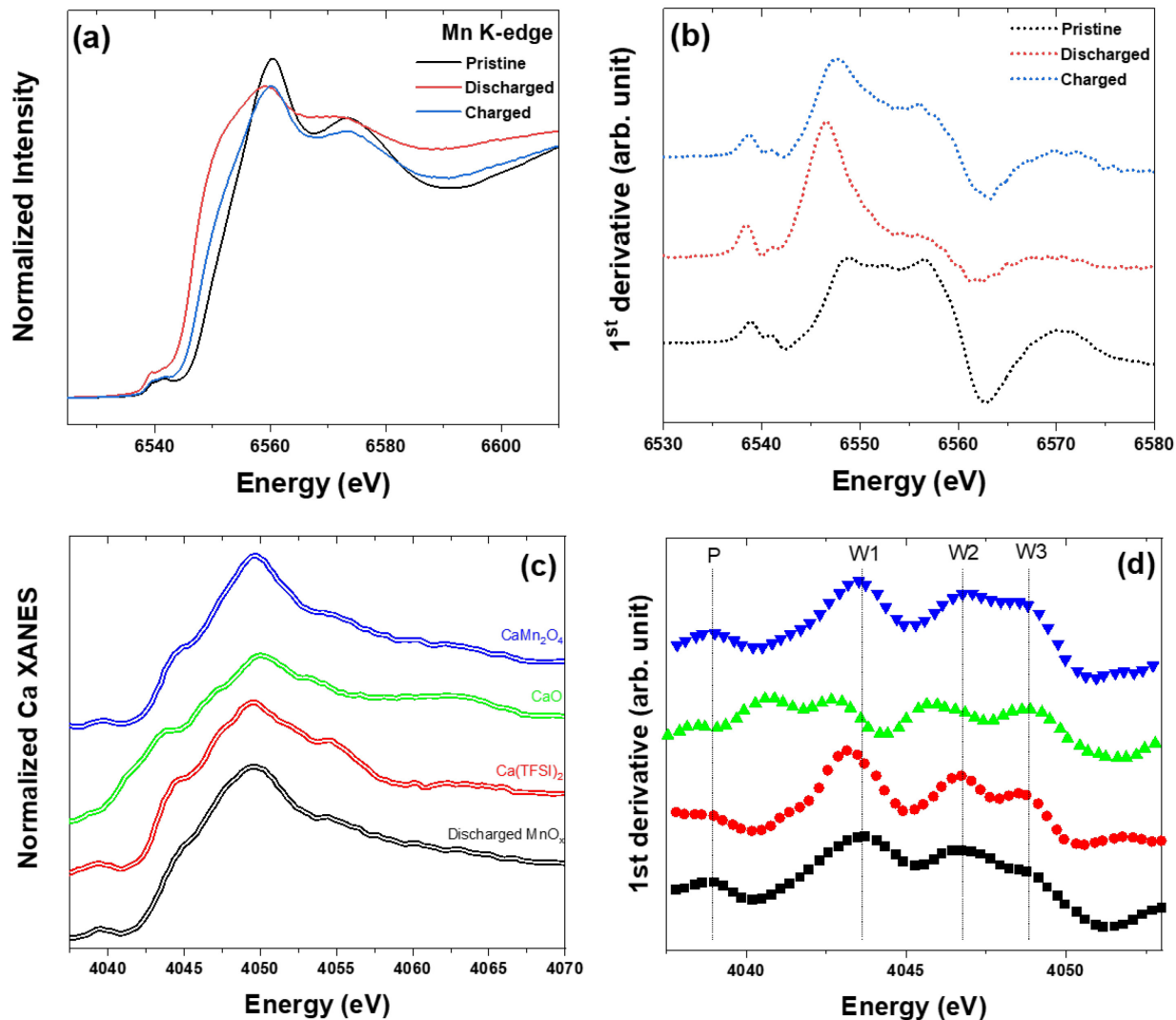
Figure 4. (a) Mn K-edge XAS and (b) corresponding first-order derivative plots of MnO_x at different states of charges prepared at 25 °C. (c) Ca K-edge XAS and (d) corresponding first-order derivative plots of discharged MnO_x (black), $Ca(TFSI)_2$ (red), CaO (green) and $CaMn_2O_4$ (blue).

Valence state of Mn and Ca at bulk. Mn K-edge X-ray absorption spectroscopy (XAS) was employed to understand the evolution of the bulk electronic environment of MnO_x as a response to electrochemical Ca^{2+} reactions. The main absorption edge involves an electronic transition from an occupied 1s level to empty valence 4p bands.[51] The position of the absorption white line is

particularly sensitive to changes in shielding of effective charges by valence electrons, enabling an estimation of a bulk-averaged oxidation state. **Figure 4a** and **b** present normalized spectra and the corresponding first derivative plots for pristine, discharged, and charged MnO_x electrodes prepared in the cell at room temperature. The integration method was used to determine the main edge position of each Mn K-edge spectra (**Figure S9**).[34] The estimated edge positions are summarized in **Table S1**. Comparing with the values of Mn oxide standards [34], the bulk oxidation state of pristine was close to around +3.6. Upon the cathodic reaction, the valence of Mn in the bulk of pristine was reduced to roughly +2.8, as manifested by a significant shift of main edge toward lower energy while the edge slope of the spectra also became less steep than pristine. The main edge of the charged state nearly shifted back to the initial position with around +3.4 oxidation state of Mn, denoting a reversible change in bulk Mn electronic states (**Figure 4a**). The results clearly showed a notable reversibility of Mn valences in the bulk by (de)intercalation of Ca^{2+}.

Ca K-edge XAS is sensitive to the local coordination of Ca^{2+} by different anions (**Figure 4c and d**). Therefore, the nature of Ca^{2+} in the discharged electrodes was assessed by comparing them with $Ca(TFSI)_2$ salt (any residuals of electrolyte), CaO (a possible byproduct of a conversion reaction), and $CaMn_2O_4$ (a standard oxide with Ca^{2+} and Mn ions in a tunnel framework, **Figure S10**). A pre-edge peak in the spectra is typically attributed to the $1s \rightarrow 3d$ transitions, which are weakly allowed when Ca does not occupy a center of inversion.[52] On the other hand, the white line consists of three main features, possibly corresponding to $1s \rightarrow 4p$ transitions,. whose relative ratio of intensity and position depends on the Ca coordination (**Figure 4d**).[52, 53] The Ca K-edge of the calciated MnO_x had a different onset of the W_1 feature and overall edge position to the spectrum

of $Ca(TFSI)_2$, as indicated in the first derivative plots (**Figure 4c** and **d**). The observed differences indicated that the Ca K-edge spectra of calciated MnO_x was not due to electrolyte impurities. Even more distinct features were observed by comparing CaO with calciated MnO_x, implying the absence of this conversion product (**Figure 4d**). The greatest similarity in the edge features was found when comparing with the spectra of $CaMn_2O_4$, an oxide containing both Ca^{2+} and Mn^{3+} in a tunnel framework. The well-matched features imply the spectrum of calciated MnO_x was most consistent with Ca^{2+} in a transition metal oxide.
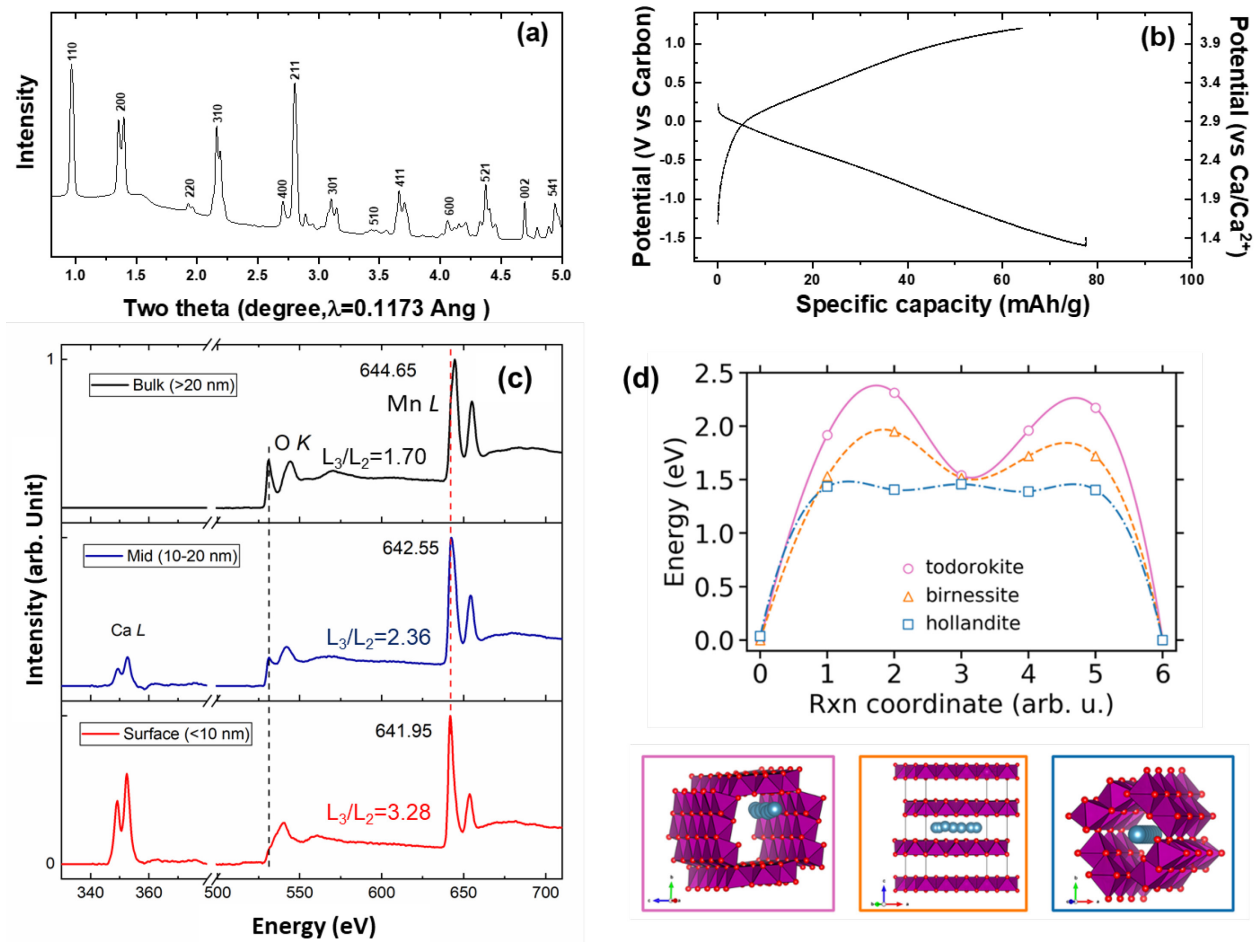
Figure 5. (a) X-ray diffraction pattern of dehydrated MnO_x and (b) potential versus capacity profiles of dehydrated MnO_x cycled in 0.5 M of $Ca(TFSI)_2$ at 25 °C. (c) EELS at different positions within a nanoparticle of the discharged dehydrated MnO_x, referred to as distance from the particle edge. (d) Energies for Ca migration in todorokite, birnessite, and hollandite using DFT calculations. The energies for Ca migration between stable sites and the dilute Ca limit are shown in the top panel. The resulting Ca migration pathways are shown in the bottom panel for todorokite, birnessite, and hollandite (left to right).

Electrochemical Ca^{2+} activity in dehydrated MnO$_x$. An oxide with a tunnel framework, a lowered H$_2$O content, and less atomic defects was prepared by calcining the as-made MnO$_x$ at 600 °C for 4 hours to evaluate the effects of lattice waters/defects (**Figure 5a**). The amount of water was estimated by thermal analysis (**Figure S11**). The loss of mass was assumed to be due to mainly the removal of water at from the lattice and the surface. Compared to the water content of the as-made MnO$_x$ (~11 % by mass), dehydrated MnO$_x$ shows a decrease with the content of ~2 % (**Figure S11**). Overall, the XRD pattern of this dehydrated MnO$_x$ indicated α-MnO$_2$ (Hollandite, 2×2 tunnel) phase (JCPDS 44-141).

The electrochemical properties of dehydrated MnO$_x$ were measured in a half-cell at C/50 at room temperature (**Figure 5b**). The discharge/charge curve of dehydrated MnO$_x$ showed the cathodic reaction proceeded from ~0 V *vs*. carbon (~2.9 V *vs*. Ca/Ca^{2+}) and a discharge capacity of ~78 mAh/g was achieved at -1.5 V *vs*. carbon (~1.4 V *vs*. Ca/Ca^{2+}). Compared to the reactivity of MnO$_x$ performed under similar electrochemical conditions, a decrease of capacity was observed. Furthermore, a distinct electrochemical profile was also observed, where the charges were accumulated along a rather linear change of the cathodic curve, leading to a higher average potential than as-made MnO$_x$. Upon subsequent charging, virtually no activity was again observed until ~0 V (*vs*. carbon) and a specific capacity of only ~65 mAh/g was obtained up to 1.2 V.

The content of Ca in the discharged state was measured by STEM-EDX (**Figure S12**). The composition was estimated by measuring multiple areas in the discharged particles. The average atomic ratio of Ca/Mn in the discharged state was around 0.04, which is significantly lower than the value of 0.13 calculated from the measured capacity (**Figure 5b** and **Figure S12**), implying the existence of secondary interfacial reactions rather than bulk intercalation. The local homogeneity of the limited Ca reaction was monitored by spatially resolved EELS (**Figure 5c**). The Ca L-edge,

O K-edge and Mn L-edge spectra were captured across the discharged particle by dividing three regions: surface, sub-surface and bulk (**Figure S13**). There was a gradual shift of the Mn L_3 peak to lower energy when moving from the surface to the bulk in a single particle, indicating that the surface was more reduced than the sub-surface and the bulk (**Figure 5c**). Moreover, the branching ratio, I_{L3}/I_{L2}, increased as it approached the surface with the evolution of the Ca L-edge signals, supporting the heterogeneity of chemical compositions. Compared to the Mn valence state on the surface of calciated as-made MnO_x (**Figure 2d**), slightly more reduced Mn states on the surface of the discharged dehydrated MnO_x electrode were observed as indicated in the branching ratios (**Figure 5c**). As shown in **Figure 5c**, the intensity of pre-edge signal, due to O $2p$-Mn $3d$ states, at the surface was lower than the bulk, implying a decrease in hybridization consistent with the formal reduction of Mn at the surface. The results of EELS at high spatial resolution strongly suggest the limited reactivity of the crystals, occurring only at the surface of dehydrated MnO_x, which is a significantly different degree of Ca^{2+} activity when compared to the properties of as-made MnO_x.

Theoretical calculation for Ca migration in polymorphs of dehydrated MnO$_2$. A possible hypothesis to explain the difference in the activity of the two oxides was sought by computing the barriers for Ca migration in dehydrated polymorphs of MnO_2 using density functional theory (DFT, **Figure 5d**). Based on the combination of the structural analyses above, three structural models were considered as representative structures for these calculations: birnessite (layered), hollandite (2×2 tunnel), and todorokite (3×3 tunnel). The constraints of DFT imposed that only versions of each phase with their ideal periodic framework and without lattice water could be sampled, thus evaluating a limiting case. Guided by the studies of cation intercalation in MnO_2,[17, 19] we sampled a variety of potential Ca intercalation sites in each phase in the dilute limit ($CaMn_{24}O_{48}$) to establish low-energy endpoints for nudged elastic band (NEB) calculations of

migration barriers. Figure 5d shows the calculated energetics and pathways for Ca migration in each dehydrated structure. For all three structures, the energy barrier for Ca migration is at least 1.4 eV, much larger than the barrier that would be required to observe dynamic intercalation of Ca, which was previously estimated to be ~500-650 meV.[2] Therefore, these results are consistent with the lack of bulk activity in the dehydrated oxide, where the complex initial structure of MnO_x collapses into crystalline hollandite (2×2 tunnel) upon calcination. This finding suggests that the enhanced activity in the as-made MnO_x is driven by the existence of lattice water and atomic defects, consistent with reports in the literature that these factors can enhance the kinetics of cation intercalation in oxides.[3, 20, 54] For example, the NEB-calculated activation barrier for Mg^{2+} hopping in $VOPO_4$ was shown to decrease from ~1.6 eV to ~0.5 eV by introducing H_2O between the $VOPO_4$ layers.[20] In order to discern between the role of the two parameters (defects and lattice water), we also attempted to perform analogous NEB calculations with varying levels of hydration in 3×3 todorokite MnO_2, but these calculations failed to converge, likely due to the complex dynamics of H_2O-assisted Ca motion inside the 3D MnO_2 tunnel structure. Further evaluation of the separate role of defects and water content should be the next steps to understand their effects on Ca mobility. Given the vast structural diversity in this family of compounds, this exploration could potentially lead to new phases with even better properties than reported here.

CONCLUSION

In this work, the capability of nanocrystals of MnO_x with crystal waters and defects to electrochemically intercalate Ca^{2+} was evaluated. The local structure was found to contain a large concentration of interlayer Mn defects, creating clustering of walls that resembled the triple chains

of todorokite. High electrochemical activity was observed in the complex oxide, with a notable degree of reversibility even at room temperature. A discharge capacity of ~130 mAhg^{-1} was delivered at room temperature which was determined by characterization of key states to correspond with structural, compositional, and redox changes that are consistent with reversible intercalation of Ca^{2+}. The observation of a virtually complete loss of activity upon dehydration and crystallization hints at the critical role of defects and lattice water within the nanocrystals in facilitating the migration of Ca^{2+}. Attempts at resolving their role indicated that crystallized, water-free polymorphs of MnO_2 suffer from very high migration barriers for Ca^{2+}, but the role of water content and defects could not be discerned with the current methodologies. Our results uncover a new candidate for a cathode in Ca-ion batteries operated by an intercalation mechanism at moderate temperatures, and cast light onto a structural family whose very high diversity makes it an attractive playground for further exploration.

Supporting Information

Supporting Information is available from of charge on the ACS Publication website. The file contains additional data discussed in the manuscript, collected by STEM, XRD, SEM, XAS, TG-DTA, and STEM.

Corresponding Author

*Email: bkwon@anl.gov, jcabana@uic.edu

Notes

The authors declare no conflict of interests.

Acknowledgments

References

1.   Gummow, R. J.; Vamvounis, G.; Kannan, M. B.; He, Y. H., Calcium-Ion Batteries: Current State-of-the-Art and Future Perspectives. *Adv. Mater.* **2018,** *30* (39).

2.   Canepa, P.; Gautam, G. S.; Hannah, D. C.; Malik, R.; Liu, M.; Gallagher, K. G.; Persson, K. A.; Ceder, G., Odyssey of Multivalent Cathode Materials: Open Questions and Future Challenges. *Chem. Rev.* **2017,** *117* (5), 4287-4341.

3.   Rong, Z. Q.; Malik, R.; Canepa, P.; Gautam, G. S.; Liu, M.; Jain, A.; Persson, K.; Ceder, G., Materials Design Rules for Multivalent Ion Mobility in Intercalation Structures. *Chem. Mater.* **2015,** *27* (17), 6016-6021.

4.   Muldoon, J.; Bucur, C. B.; Gregory, T., Quest for Nonaqueous Multivalent Secondary Batteries: Magnesium and Beyond. *Chem. Rev.* **2014,** *114* (23), 11683-11720.

5.   Ponrouch, A.; Frontera, C.; Barde, F.; Palacin, M. R., Towards a calcium-based rechargeable battery. *Nat. Mater.* **2016,** *15* (2), 169-172.

6.   Arroyo-de Dompablo, M. E.; Krich, C.; Nava-Avendano, J.; Biskup, N.; Palacin, M. R.; Barde, F., A Joint Computational and Experimental Evaluation of $CaMn_2O_4$ Polymorphs as Cathode Materials for Ca Ion Batteries. *Chem. Mater.* **2016,** *28* (19), 6886-6893.

7.   Liu, M.; Rong, Z. Q.; Malik, R.; Canepa, P.; Jain, A.; Ceder, G.; Persson, K. A., Spinel compounds as multivalent battery cathodes: a systematic evaluation based on ab initio calculations. *Energ. Environ. Sci.* **2015,** *8* (3), 964-974.

8.   Xu, X. M.; Duan, M. Y.; Yue, Y. F.; Li, Q.; Zhang, X.; Wu, L.; Wu, P. J.; Song, B.; Mai, L. Q., Bilayered $Mg_{0.25}V_2O_5 \cdot H_2O$ as a Stable Cathode for Rechargeable Ca-Ion Batteries. *ACS Energy Lett.* **2019,** *4* (6), 1328-1335.

9.   Lipson, A. L.; Pan, B. F.; Lapidus, S. H.; Liao, C.; Vaughey, J. T.; Ingram, B. J., Rechargeable Ca-Ion Batteries: A New Energy Storage System. *Chem. Mater.* **2015,** *27* (24), 8442-8447.

10.   Park, J.; Xu, Z. L.; Yoon, G.; Park, S. K.; Wang, J.; Hyun, H.; Park, H.; Lim, J.; Ko, Y. J.; Yun, Y. S.; Kang, K., Stable and High-Power Calcium-Ion Batteries Enabled by Calcium Intercalation into Graphite. *Adv. Mater.* **2020,** *32* (4).

11.   Tchitchekova, D. S.; Ponrouch, A.; Verrelli, R.; Broux, T.; Frontera, C.; Sorrentino, A.; Barde, F.; Biskup, N.; Arroyo-de Dompablo, M. E.; Palacin, M. R., Electrochemical Intercalation of Calcium and Magnesium in TiS2: Fundamental Studies Related to Multivalent Battery Applications. *Chem. Mater.* **2018,** *30* (3), 847-856.

12.   Verrelli, R.; Black, A.; Dugas, R.; Tchitchekova, D.; Ponrouch, A.; Palacin, M. R., Steps Towards the Use of TiS_2 Electrodes in Ca Batteries. *J. Electrochem. Soc.* **2020,** *167* (7).

13.   Arroyo-de Dompablo, M. E.; Ponrouch, A.; Johansson, P.; Palacin, M. R., Achievements, Challenges, and Prospects of Calcium Batteries. *Chem. Rev.* **2020,** *120* (14), 6331-6357.

14.   Sun, X. Q.; Bonnick, P.; Nazar, L. F., Layered TiS2 Positive Electrode for Mg Batteries. *ACS Energy Lett.* **2016,** *1* (1), 297-301.

15.   Arroyo-de Dompablo, M. E.; Krich, C.; Nava-Avendano, J.; Palacin, M. R.; Barde, F., In quest of cathode materials for Ca ion batteries: the $CaMO_3$ perovskites (M = Mo, Cr, Mn, Fe, Co, and Ni). *Phys. Chem. Chem. Phys.* **2016,** *18* (29), 19966-19972.

16.   Li, Z. Y.; Fuhr, O.; Fichtner, M.; Zhao-Karger, Z., Towards stable and efficient electrolytes for room-temperature rechargeable calcium batteries. *Energ. Environ. Sci.* **2019,** *12* (12), 3496-3501.

17.   Hu, X. B.; Kitchaev, D. A.; Wu, L. J.; Zhang, B. J.; Meng, Q. P.; Poyraz, A. S.; Marschilok, A. C.; Takeuchi, E. S.; Takeuchi, K. J.; Ceder, G.; Zhu, Y. M., Revealing and Rationalizing the Rich Polytypism of Todorokite MnO_2. *J. Am. Chem. Soc.* **2018,** *140* (22), 6961-6968.

18.   Kitchaev, D. A.; Dacek, S. T.; Sun, W. H.; Ceder, G., Thermodynamics of Phase Selection in MnO_2 Framework Structures through Alkali Intercalation and Hydration. *J. Am. Chem. Soc.* **2017,** *139* (7), 2672-2681.

19.   Birkner, N.; Navrotsky, A., Thermodynamics of manganese oxides: Sodium, potassium, and calcium birnessite and cryptomelane. *P. Natl. Acad. Sci. USA* **2017,** *114* (7), E1046-E1053.

20.   Ji, X.; Chen, J.; Wang, F.; Sun, W.; Ruan, Y. J.; Miao, L.; Jiang, J. J.; Wang, C. S., Water-Activated $VOPO_4$ for Magnesium Ion Batteries. *Nano. Lett.* **2018,** *18* (10), 6441-6448.

21.   Sai Gautam, G.; Canepa, P.; Richards, W. D.; Malik, R.; Ceder, G., Role of Structural H_2O in Intercalation Electrodes: The Case of Mg in Nanocrystalline Xerogel-V_2O_5. *Nano Lett* **2016,** *16* (4), 2426-31.

22.   Kwon, B. J.; Kim, C.; Jokisaari, J. R.; Yoo, H. D.; Han, S. D.; Kim, S.; Lau, K. C.; Liao, C.; Liu, Y. S.; Guo, J. H.; Key, B.; Klie, R. F.; Cabana, J., Intercalation of Mg into a Few-Layer Phyllomanganate in Nonaqueous Electrolytes at Room Temperature. *Chem. Mater.* **2020,** *32* (14), 6014-6025.

23.   Han, S. D.; Kim, S.; Li, D. G.; Petkov, V.; Yoo, H. D.; Phillips, P. J.; Wang, H.; Kim, J. J.; More, K. L.; Key, B.; Klie, R. F.; Cabana, J.; Stamenkovic, V. R.; Fister, T. T.; Markovic, N. M.; Burrell, A. K.; Tepavcevic, S.; Vaughey, J. T., Mechanism of Zn Insertion into Nanostructured delta-MnO_2: A Nonaqueous Rechargeable Zn Metal Battery. *Chem. Mater.* **2017,** *29* (11), 4874-4884.

24.   Hyoung, J.; Heo, J. W.; Hong, S. T., Investigation of electrochemical calcium-ion energy storage mechanism in potassium birnessite. *J. Power Sources* **2018,** *390*, 127-133.

25.   Hu, L. H.; Jokisaari, J. R.; Kwon, B. J.; Yin, L.; Kim, S.; Park, H.; Lapidus, S. H.; Klie, R. F.; Key, B.; Zapol, P.; Ingram, B. J.; Vaughey, J. T.; Cabana, J., High Capacity for Mg^{2+} Deintercalation in Spinel Vanadium Oxide Nanocrystals. *ACS Energy Lett.* **2020,** *5* (8), 2721-2727.

26.   Hu, L. H.; Johnson, I. D.; Kim, S.; Nolis, G. M.; Freeland, J. W.; Yoo, H. D.; Fister, T. T.; McCafferty, L.; Ashton, T. E.; Darr, J. A.; Cabana, J., Tailoring the electrochemical activity of magnesium chromium oxide towards Mg batteries through control of size and crystal structure. *Nanoscale* **2019,** *11* (2), 639-646.

27.   Drits, V. A.; Lanson, B.; Gaillot, A. C., Birnessite polytype systematics and identification by powder X-ray diffraction. *Am. Mineral* **2007,** *92* (5-6), 771-788.

28.   Feng, X. H.; Tan, W. F.; Liu, F.; Wang, J. B.; Ruan, H. D., Synthesis of todorokite at atmospheric pressure. *Chem. Mater.* **2004,** *16* (22), 4330-4336.

29.   Morando, C.; Cofrancesco, P.; Tealdi, C., Zn ion diffusion in spinel-type cathode materials for rechargeable batteries: the role of point defects. *Mater. Today Commun.* **2020,** *25*.

30.   Orikasa, Y.; Kisu, K.; Iwama, E.; Naoi, W.; Yamaguchi, Y.; Yamaguchi, Y.; Okita, N.; Ohara, K.; Munesada, T.; Hattori, M.; Yamamoto, K.; Rozier, P.; Simon, P.; Naoi, K., Noncrystalline Nanocomposites as a Remedy for the Low Diffusivity of Multivalent Ions in Battery Cathodes. *Chem. Mater.* **2020,** *32* (3), 1011-1021.

31.   Kresse, G.; Furthmuller, J., Efficiency of ab-initio total energy calculations for metals and semiconductors using a plane-wave basis set. *Comp. Mater. Sci.* **1996,** *6* (1), 15-50.

32.   Kitchaev, D. A.; Peng, H. W.; Liu, Y.; Sun, J. W.; Perdew, J. P.; Ceder, G., Energetics of MnO_2 polymorphs in density functional theory. *Phys. Rev. B* **2016,** *93* (4).

33.   P. J. Chupas, X. Q., J. C. Hanson, P. L. Lee, C. P. Grey and S. J. L. Billinge, Rapid-acquisition pair distribution function (RA-PDF) analysis. *J. Appl. Crystallogr.* **2003,** *36* (6), 1342-1347.

34.   Dau, H.; Liebisch, P.; Haumann, M., X-ray absorption spectroscopy to analyze nuclear geometry and electronic structure of biological metal centers - Potential and questions examined with special focus on the tetra-nuclear manganese complex of oxygenic photosynthesis. *Anal. Bioanal. Chem.* **2003,** *376* (5), 562-583.

35.   Dugas, R.; Forero-Saboya, J. D.; Ponrouch, A., Methods and Protocols for Reliable Electrochemical Testing in Post-Li Batteries (Na, K, Mg, and Ca). *Chem. Mater.* **2019,** *31* (21), 8613-8628.

36.   Xu, J. J.; Kinser, A. J.; Owens, B. B.; Smyrl, W. H., Amorphous manganese dioxide: A high capacity lithium intercalation host. *Electrochem. Solid. St.* **1998,** *1* (1), 1-3.

37.   Manceau, A.; Marcus, M. A.; Grangeon, S.; Lanson, M.; Lanson, B.; Gaillot, A. C.; Skanthakumar, S.; Soderholm, L., Short-range and long-range order of phyllomanganate nanoparticles determined using high-energy X-ray scattering. *J. Appl. Crystallogr.* **2013,** *46*, 193-209.

38.   Lee, S.; Xu, H. F.; Xu, W. Q.; Sun, X. M., The structure and crystal chemistry of vernadite in ferromanganese crusts. *Acta Crystallogr. B* **2019,** *75*, 591-598.

39.   Grangeon, S.; Fernandez-Martinez, A.; Warmont, F.; Gloter, A.; Marty, N.; Poulain, A.; Lanson, B., Cryptomelane formation from nanocrystalline vernadite precursor: a high energy X-ray scattering and transmission electron microscopy perspective on reaction mechanisms. *Geochem. T.* **2015,** *16*.

40.   Atkins, A. L.; Shaw, S.; Peacock, C. L., Nucleation and growth of todorokite from birnessite: Implications for trace-metal cycling in marine sediments. *Geochim. Cosmochim. Ac.* **2014,** *144*, 109-125.

41.   Turner, S.; Buseck, P. R., Todorokites - a New Family of Naturally-Occurring Manganese Oxides. *Science* **1981,** *212* (4498), 1024-1027.

42.   Ruch, P. W.; Cericola, D.; Hahn, M.; Kotz, R.; Wokaun, A., On the use of activated carbon as a quasi-reference electrode in non-aqueous electrolyte solutions. *J. Electroanal. Chem.* **2009,** *636* (1-2), 128-131.

43.   X. Liu, G. A. E., S. Passerini, Evaluation of counter and reference electrodes for the investigation of Ca battery materials. *J. Power Sources Advances* **2020,** *2*, 100008.

44.   Kim, S.; Yin, L.; Lee, M. H.; Parajuli, P.; Blanc, L.; Fister, T. T.; Park, H.; Kwon, B. J.; Ingram, B. J.; Zapol, P.; Klie, R. F.; Kang, K.; Nazar, L. F.; Lapidus, S. H.; Vaughey, J. T., High-Voltage Phosphate Cathodes for Rechargeable Ca-Ion Batteries. *ACS Energy Lett.* **2020,** *5* (10), 3203-3211.

45.   Nolis, G. M.; Adil, A.; Yoo, H. D.; Hu, L. H.; Bayliss, R. D.; Lapidus, S. H.; Berkland, L.; Phillips, P. J.; Freeland, J. W.; Kim, C.; Klie, R. F.; Cabana, J., Electrochemical Reduction of a Spinel-Type Manganese Oxide Cathode in Aqueous Electrolytes with Ca^{2+} or Zn^{2+}. *J. Phys. Chem. C* **2018,** *122* (8), 4182-4188.

46.   Liu, R. S.; Jang, L. Y.; Chen, J. M.; Tsai, Y. C.; Hwang, Y. D.; Liu, R. G., X-ray absorption studies in spinel-type $LiMn_2O_4$. *J. Solid. State. Chem.* **1997,** *128* (2), 326-329.

47.   Rez, P.; Blackwell, A., Ca L$_{23}$ Spectrum in Amorphous and Crystalline Phases of Calcium Carbonate. *J. Phys. Chem. B* **2011,** *115* (38), 11193-11198.

48.   Liu, J.; Yu, L.; Hu, E. Y.; Guiton, B. S.; Yang, X. Q.; Page, K., Large-Scale Synthesis and Comprehensive Structure Study of delta-MnO$_2$. *Inorg. Chem.* **2018,** *57* (12), 6873-6882.

49.   Jung, H.; Taillefert, M.; Sun, J. Y.; Wang, Q.; Borkiewicz, O. J.; Liu, P.; Yang, L. F.; Chen, S.; Chen, H. L.; Tang, Y. Z., Redox Cycling Driven Transformation of Layered Manganese Oxides to Tunnel Structures. *J. Am. Chem. Soc.* **2020,** *142* (5), 2506-2513.

50.   Reed, J.; Ceder, G., Role of electronic structure in the susceptibility of metastable transition-metal oxide structures to transformation. *Chem. Rev.* **2004,** *104* (10), 4513-33.

51.   Kim, C.; Phillips, P. J.; Key, B.; Yi, T. H.; Nordlund, D.; Yu, Y. S.; Bayliss, R. D.; Han, S. D.; He, M. N.; Zhang, Z. C.; Burrell, A. K.; Klie, R. F.; Cabana, J., Direct Observation of Reversible Magnesium Ion Intercalation into a Spinel Oxide Host. *Adv. Mater.* **2015,** *27* (22), 3377-3384.

52.   Martin-Diaconescu, V.; Gennari, M.; Gerey, B.; Tsui, E.; Kanady, J.; Tran, R.; Pecaut, J.; Maganas, D.; Krewald, V.; Goure, E.; Duboc, C.; Yano, J.; Agapie, T.; Collomb, M. N.; DeBeer, S., Ca K-Edge XAS as a Probe of Calcium Centers in Complex Systems. *Inorg. Chem.* **2015,** *54* (4), 1283-1292.

53.   Kim, T. H.; Heo, I.; Paek, S. M.; Park, C. B.; Choi, A. J.; Lee, S. H.; Choy, J. H.; Oh, J. M., Layered Metal Hydroxides Containing Calcium and Their Structural Analysis. *B. Korean Chem. Soc.* **2012,** *33* (6), 1845-1850.

54.   Gautam, G. S.; Canepa, P.; Urban, A.; Bo, S. H.; Ceder, G., Influence of Inversion on Mg Mobility and Electrochemistry in Spinels. *Chem. Mater.* **2017,** *29* (18), 7918-7930.